Computational Study of Electromagnetic Fields, Eddy Currents and Induction Heating in Thin and Thick Workpieces

Mohammad Hossein Tavakoli*, Hossein Karbaschi and Feridoun Samavat

Physics Department, Bu-Ali Sina University, Hamedan 65174, Iran.

Abstract. A set of 2D steady state finite element numerical simulations of electromagnetic fields, eddy currents distribution and induction heating pattern has been done for different thicknesses of a metal workpiece. Comparison between the calculation results show the importance of workpiece thickness on induction heating process including electromagnetic field distribution, eddy currents pattern, heating structure and coil efficiency.

PACS: 02.60.Cb, 02.70.Dh, 07.05.Tp, 81.05.Bx

Key words: Computer simulation, finite element analysis, modeling, induction heating, metals.

1 Introduction

Radio frequency induction heating is the process of heating an electrically conducting material (usually a metal) by electromagnetic induction, where eddy currents are generated within the workpiece and resistance leads to Joulean heating (I^2R) of the material in the form of temporal and spatial volumetric heating. Since induction heating is a non-contact process, the heating process does not contaminate the material being heated. Because the power goes directly into the heated metal, the process is clean, fast, repeatable, relatively efficient, and allows automatic control. This can be contrasted with other heating methods where heat is generated in a flame or heating element, which is then applied to the workpiece. For these reasons induction heating leads itself to some unique applications in industry and material processing.

*Corresponding author. *Email addresses:* `mht@basu.ac.ir` (M. H. Tavakoli), `H.Karbaschi@gmail.com` (H. Karbaschi), `fsamavat@yahoo.com` (F. Samavat)

An induction heating installation has three important parts: the electrical power source for generation of high-frequency energy, the work coil (RF-coil) and the workpiece (metallic material) where the final transfer of the electrical energy into required heat is occurred. The RF-coil must establish suitable electromagnetic flux lines in the workpiece and this field must be powerful enough to do the job such as joining, treating, heating and testing. The frequency of alternative electrical current used depends on the object size, material type, penetration depth and coupling between the work coil and the object to be heated. In this aspect, the amount of induced eddy currents and power as well as their spatial distribution in the workpiece are the major parameters to be determined. Understanding the physics of these properties is quite crucial and important when designing induction heating systems.

Mathematical modelling combined with computer simulation is a powerful tool for induction heating design and optimization, induction coil design, equipment selection, as well as education and business presentations. The traditional approaches to induction heating system development were based on a pure "trial and error" method. These traditional methods for induction coil and process design were time consuming and expensive due to having to manufacture and modify several inductors. These methods were also limited in applied cases and could not provide the developer with a good understanding of what is going on in a given induction heating system or information on why a given induction system worked or did not work properly. Today, more and more induction heating designers are shifting their development process from traditional empirical methods to computer simulation or a combination of both. Computer simulation provides induction process designers with a wealth of information on the system dynamics. It also can be used to explain, demonstrate and predict the process sensitivity to changes of an induction system. The early mathematical models of induction heating involved closed form analytical expressions [1–5]. The extensive majority of induction heating have been modeled using the finite difference method (FDM) [6–8], the finite element method (FEM) [9–16], the boundary element method (BEM) [17–19], the hybrid FEM-BEM method [20–23] and the impedance boundary condition (IBC) [24–29]. Over the past 30 years, the numerical treatment of induction processes has developed to the point where, today, there are numerous software packages available commercially, some of which include capabilities to treat complex problems in which electromagnetic fields are coupled to material properties, thermal process, and mechanical deformations.

In this article, we try to investigate the effects of workpiece thickness on the strength and distribution of the electromagnetic fields, eddy currents and heat generation in the setup. To do it, different thicknesses of a cylindrical steel workpiece (i.e. tiny, thin and thick) are considered corresponding to real applications of the RF-heating system.

2 Mathematical model

2.1 Governing equations

For calculating an electromagnetic field it is necessary to solve Maxwell's equations [30–32]. In order to solve these equations for our purpose, we have to make several assumptions: (1) the system is rotationally symmetric about the z-axis, i.e., all quantities are independent of the azimuthal coordinate ϕ, (2) all materials are isotropic, non-magnetic and have no net electric charge, (3) the displacement current is neglected, (4) the distribution of electrical current (also voltage) in the RF-coil is uniform, (5) the self-inductance effect in the RF-coil is taken into account, (6) the currents (impressed and induced) have a steady state quality and as a result the electromagnetic field quantities are harmonically oscillating functions with a fixed single frequency.

Under these assumptions, Maxwell's equations in differential form and in the "mks" units (meter-kilogram-second-coulomb) can be written as:

$$\nabla \cdot \mathbf{E} = 0, \quad \text{(from Gauss's law)} \tag{2.1}$$

$$\nabla \cdot \mathbf{B} = 0, \quad \text{(from Gauss's law)} \tag{2.2}$$

$$\nabla \times \mathbf{B} = \mu \mathbf{J}, \quad \text{(from Ampere's law)} \tag{2.3}$$

$$\nabla \times \mathbf{E} = -\frac{\partial \mathbf{B}}{\partial t}, \quad \text{(from Faraday's law)} \tag{2.4}$$

$$\mathbf{J} = \sigma \mathbf{E}, \tag{2.5}$$

where $\mathbf{E}$ is the electric field intensity, $\mathbf{B}$ is the magnetic flux density, $\mathbf{J}$ is the free charge current density, μ is the magnetic permeability and σ is the electrical conductivity of the medium, which is a non-zero value only in metallic parts.

Introducing the vector potential $\mathbf{A}$ as

$$\mathbf{B} = \nabla \times \mathbf{A} \tag{2.6}$$

and assuming axi-symmetric condition, we can transform Eqs. (2.1)-(2.5) into a simple scalar equation [33, 34]

$$\frac{\partial}{\partial r} \left(\frac{1}{r} \frac{\partial \Psi_B}{\partial r} \right) + \frac{\partial}{\partial z} \left(\frac{1}{r} \frac{\partial \Psi_B}{\partial z} \right) = -\mu J_\phi \tag{2.7}$$

in which Ψ_B is the *magnetic stream function* defined by $\Psi_B(r,z,t) \equiv r A_\phi(r,z,t)$, where A_ϕ is the azimuthal component of $\mathbf{A}$ and (r,ϕ,z) is the cylindrical coordinates. In other words, we assume that all currents (driving and induced) flow only in the azimuthal direction both in the coil and the workpiece.

If we include the self-inductance effect in the induction coil as eddy currents represented by $J_e = -(\sigma_{co}/r)(\partial \Psi_B/\partial t)$, then

$$J_\phi = \begin{cases} J_d + J_e = J_d - \dfrac{\sigma_{co}}{r}\dfrac{\partial \Psi_B}{\partial t} & \text{driving and eddy currents in the coil,} \\[4mm] J_e = -\dfrac{\sigma_w}{r}\dfrac{\partial \Psi_B}{\partial t} & \text{eddy currents in the workpiece,} \end{cases} \tag{2.8}$$

where σ_{co} and σ_w are the electrical conductivity of the RF-coil and workpiece, respectively. Setting $J_d = J_0 \cos\omega t$ as the driving current in the coil we can find a solution of the form

$$\Psi_B(r,z,t) = C(r,z)\cos\omega t + S(r,z)\sin\omega t, \tag{2.9}$$

where $C(r,z)$ is the in-phase component and $S(r,z)$ is the out-of-phase component of the solution.

Now the coupled set of elliptic PDE's for $C(r,z)$ and $S(r,z)$ is:

$$\frac{\partial}{\partial r}\left(\frac{1}{r}\frac{\partial C}{\partial r}\right) + \frac{\partial}{\partial z}\left(\frac{1}{r}\frac{\partial C}{\partial z}\right) = \begin{cases} -\mu_{co}\left(J_0 - \dfrac{\sigma_{co}\omega}{r}S\right) & \text{coil,} \\ \dfrac{\mu_w\sigma_w\omega}{r}S & \text{workpiece,} \\ 0 & \text{elsewhere,} \end{cases} \tag{2.10}$$

$$\frac{\partial}{\partial r}\left(\frac{1}{r}\frac{\partial S}{\partial r}\right) + \frac{\partial}{\partial z}\left(\frac{1}{r}\frac{\partial S}{\partial z}\right) = \begin{cases} -\mu_{co}\dfrac{\sigma_{co}\omega}{r}C & \text{coil,} \\ -\dfrac{\mu_w\sigma_w\omega}{r}C & \text{workpiece,} \\ 0 & \text{elsewhere.} \end{cases} \tag{2.11}$$

After solving (2.10) and (2.11) for $C(r,z)$ and $S(r,z)$, the eddy currents distribution and the energy dissipation rate can be computed via

$$\begin{aligned} J_e &= \frac{\sigma_w\omega}{r}\left(C(r,z)\sin\omega t - S(r,z)\cos\omega t\right) \\ &= J_S\sin\omega t + J_C\cos\omega t \end{aligned} \tag{2.12}$$

and

$$P(r,z,t) = \frac{J_\phi^2}{\sigma} \tag{2.13}$$

$$= \begin{cases} \dfrac{\sigma_{co}\omega^2}{r^2}\left[C^2\sin^2\omega t + \left(\dfrac{J_0 r}{\sigma_{co}\omega} - S\right)^2\cos^2\omega t + C\left(\dfrac{J_0 r}{\sigma_{co}\omega} - S\right)\sin 2\omega t\right] & \text{coil,} \\ \dfrac{\sigma_w\omega^2}{r^2}\left(C^2\sin^2\omega t + S^2\cos^2\omega t - CS\sin 2\omega t\right) & \text{workpiece.} \end{cases}$$

Thus, the power is generated in all metallic parts (including RF-coil) as a function of 2ω. The period for this time-dependence is $\tau = 2\pi/\omega = 10^{-4}$ s for a 10 kHz induction system. Since the time-harmonic function is so short, representation of the heat generation by the time averaged quantity is more useful, which we average over one period to obtain the

volumetric heat generation rate,

$$
\begin{aligned}
q(r,z) &= \frac{\omega}{2\pi} \int_0^{2\pi/\omega} P(r,z,t)\ \mathrm{d}t \\
&= \begin{cases}
\dfrac{\sigma_{co}\omega^2}{2r^2}\left[C^2 + \left(\dfrac{J_0 r}{\sigma_{co}\omega} - S \right)^2 \right] & \text{coil,} \\[4mm]
\dfrac{\sigma_w \omega^2}{2r^2}(C^2 + S^2) & \text{workpiece.}
\end{cases}
\end{aligned}
\tag{2.14}
$$

The boundary conditions are $\Psi_B = 0$; both in the far field $(r,z \to \infty)$ and at the axis of symmetry $(r=0)$.

The involved partial differential equations require using a numerical discretization method to solve them. The calculation of the fundamental equations with boundary conditions has been made with 2D finite element method. After solving the set of equations we can obtain the electromagnetic field and eddy currents distribution as well as the power densities in all parts of the studied system.

Table 1: Values of electrical conductivity (mho/cm) used in our calculations; the subscripts co and w denote coil (*copper*) and workpiece (*steel*), respectively.

Symbol	Value
σ_{co}	5.9×10^5
σ_w	4.0×10^4

2.2 The calculation conditions

Values of electrical conductivity employed for our calculations are presented in Table 1 and operating parameters are listed in Table 2. We consider the following setup: A right cylindrical conductor load (i.e. steel workpiece) in the direction of Oz (i.e. Oz is the centerline). This workpiece is surrounded by a multiturn cylindrical induction coil with 6 hollow rectangular-shaped copper turns, Fig. 1. In a real induction system this coil is usually cooled very efficiently by water flowing inside the coil turns. Therefore it is realistic to assume that the coil is always at room temperature. We assume a total voltage of the coil $V_{coil} = 200\ v$ with a frequency of 10 kHz. The driving current density in the induction coil is calculated by $J_0 = \sigma_{co} V_{coil} / (2\pi R_{co} N)$, where R_{co} is the mean value of the coil radius and N is the number of coil turns. For the magnetic permeability (μ) we assume that it is everywhere the constant value of free space $\mu = \mu_r \mu_0 \simeq \mu_0$ (i.e. $\mu_r \simeq 1$) where μ_r is the relative magnetic permeability.

The quantity $\delta_w = (2/\mu_w \sigma_w \omega)^{1/2}$ has the dimension of a length and is called the *skin depth* (or penetration depth). It is a measure of the field penetration depth into the conductors. In our calculation the corresponding skin depth of the steel workpiece is $\delta_w = 2.5\ mm$. For the metal workpiece, different thicknesses are considered compared to

Table 2: Operating parameters used for calculations.

Description (units)	Symbol	Value
Workpiece outer radius (*mm*)	r_w	50
Workpiece thickness (*mm*)	l_w	2,5,10,55
Workpiece height (*mm*)	h_w	186
Coil inner radius (*mm*)	r_{co}	85
Coil width (*mm*)	l_{co}	10
Coil wall thickness (*mm*)	l_{co}	1
Height of coil turns (*mm*)	h_{co}	13
Distance between coil turns (*mm*)	d_{co}	3
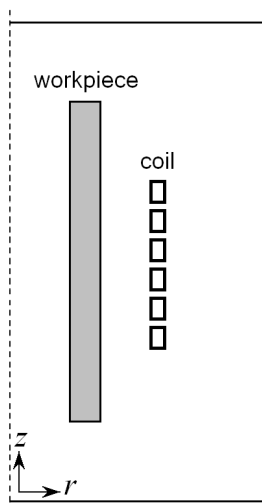
Figure 1: Sketch of the induction heating setup including a right cylindrical workpiece and a multiturn RF-coil.

corresponding skin depth, tiny ($l_w = 2\ mm < \delta_w$), thin ($l_w = 5\ mm < 3\delta_w$) and thick ($l_w = 10$ and $55\ mm > 3\delta_w$).

It should be mentioned here that since induction heating is a very complicated process, we can not expect accurate simulation of the whole chain of coupled phenomena — electromagnetic, thermal, mechanical, hydrodynamic and metallurgical — during a heating process. The most important and controllable process is electromagnetic which is analyzed here.

The results based on this set of parameters will be presented now.

3   Results and discussion

We explain the results of induced electromagnetic fields, eddy currents distribution and power pattern in a RF-heating setup including an induction coil and a cylindrical workpiece with different thicknesses ($l_w = 2,5,10,55\ mm$) and unique hight.
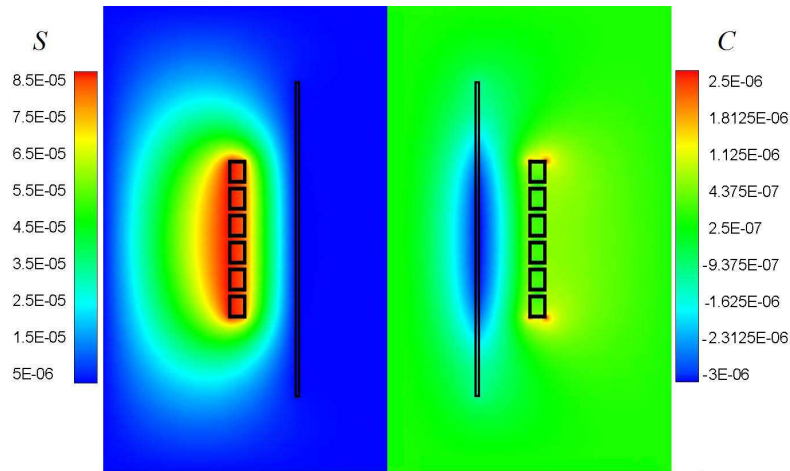
Figure 2: Components of the magnetic stream function (Ψ_B) calculated for the case of $l_w = 2\ mm$ (tiny) workpiece thickness. The right hand side shows the in-phase component (C) with $C_{max} = 3.0 \times 10^{-6}$ *weber* on the lowest and top edges of the RF-coil and $C_{min} = -3.3 \times 10^{-6}$ *weber* on the middle of the workpiece outer surface. The left hand side shows the out-of-phase component (S) with $S_{max} = 9.0 \times 10^{-5}$ *weber* on the outer surfaces of the induction coil turns.
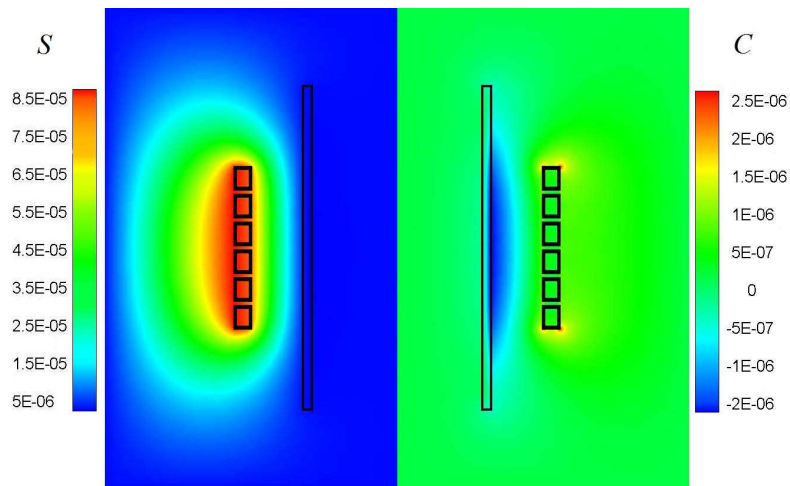
Figure 3: Components of the magnetic stream function (Ψ_B) calculated for the case of $l_w = 5\ mm$ (thin) workpiece thickness. The right hand side shows the in-phase component with $C_{max} = 3.0 \times 10^{-6}$ *weber* and $C_{min} = -2.4 \times 10^{-6}$ *weber*. The left hand side shows the out-of-phase component with $S_{max} = 9.0 \times 10^{-5}$ *weber*.

3.1 Electromagnetic field distribution

The starting point for our study is a tiny sample cylindrical workpiece with a 2 *mm* thickness. Fig. 2 shows the distribution of in-phase component (right hand side) and out-of-phase component (left hand side) of the magnetic stream function for this case. The maximum of in-phase component (C) is located at the lowest and top edges of the RF-coil
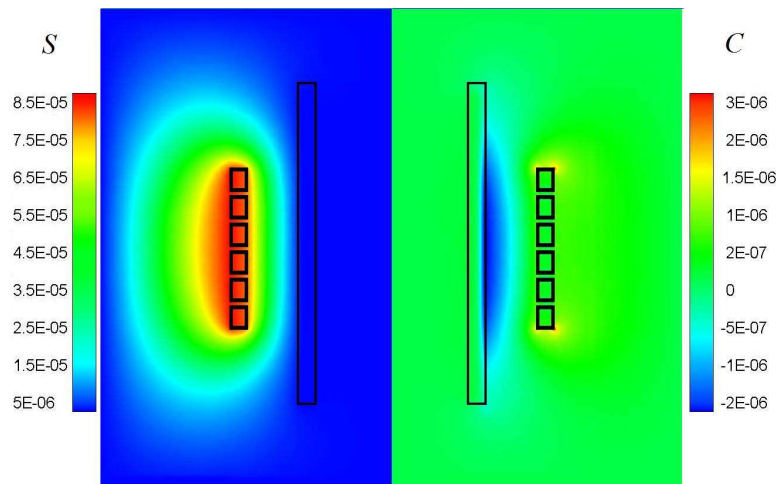
Figure 4: Components of the magnetic stream function (Ψ_B) calculated for the case of $l_w = 10$ mm workpiece thickness. The right hand side shows the in-phase component with $C_{max} = 3.3 \times 10^{-6}$ weber and $C_{min} = -2.4 \times 10^{-6}$ weber. The left hand side shows the out-of-phase component with $S_{max} = 9.0 \times 10^{-5}$ weber.
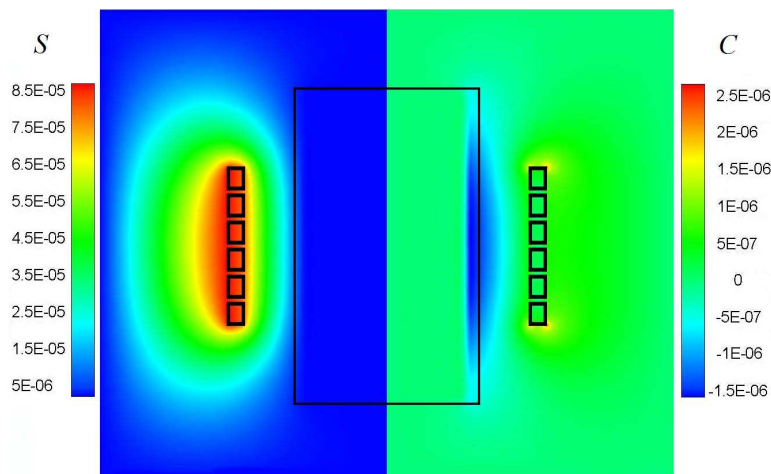
Figure 5: Components of the magnetic stream function (Ψ_B) calculated for the case of $l_w = 55$ mm (thick) workpiece thickness. The right hand side shows the in-phase component with $C_{max} = 3.3 \times 10^{-6}$ weber and $C_{min} = -2.4 \times 10^{-6}$ weber. The left hand side shows the out-of-phase component with $S_{max} = 9.0 \times 10^{-5}$ weber.

$(C_{max} = 3.0 \times 10^{-6}$ weber$)$ while the minimum $(C_{min} = -3.30 \times 10^{-6}$ weber$)$ is located on the middle of the outer surface of workpiece. For the out-of-phase component (S), the maximum is located at the outer surfaces of the induction coil turns $(S_{max} = 9.0 \times 10^{-5}$ weber$)$ and its distribution has a linear gradient in the space between the coil and the workpiece. The workpiece tends to force the electromagnetic field components out of its body and makes them more intense in the space between the workpiece and the coil compared to other places.

It is interesting to note that both components are quite small and also $|S/C| \sim 1$ in the workpiece where the required heat generation occurs. As a result, both components take part in the required heat generation equally, according to Eq. (2.14).

Figs. 3-5 illustrate the spatial distribution of in-phase and out-of-phase components of the magnetic stream function for the cases of $l_w = 5, 10$ and $55\ mm$ workpiece thickness, respectively. Some interesting advantages are,

• Although the distribution and intensity of the S-field component is clearly similar in all cases but this is not true for the C-field component. The C-field intensity vanishes rapidly in the workpiece area with increasing its thickness (l_w), i.e., the C-field intensity has a large gradient in the thick workpieces. On the other side, although C_{max} remains approximately constant but $|C_{min}|$ decreases with increasing the workpiece thickness.

• Deformation and distortion of the C-component in the area close to the top and bottom edges of the workpiece and RF-coil is particularly evident for all cases (edge effect). This distortion is stronger for the workpiece corners in the case of $l_w = 2\ mm$ (tiny workpiece).

• Distribution of the in-phase component (C) depends on the geometry of both induction coil and workpiece, while the out-of-phase component (S) mainly depends on the configuration of RF-coil where the driving current is produced.

3.2 Eddy currents distribution

Fig. 6 shows the distribution of in-phase component and out-of-phase component of the eddy currents (i.e. J_C and J_S) in the workpiece for the cases of $l_w = 2, 5, 10$ and $55\ mm$, respectively. Some interesting aspects are as follow,

• It is seen that the distributions of both components have a damped wave shape which is a result of propagation of electromagnetic wave in the conductor workpiece [35], Fig. 7.

• Both components are always in the opposite direction to the driving current J_0 (because $J_C < 0$ and $J_S < 0$) on the outer surface of the workpiece side wall.

• In all cases, both J_C^{min} and J_S^{min} are located on the middle of the outer surface of the workpiece side wall. J_S^{min} shows the related wave crest which is not true for J_C^{min}.

• Although the position of J_S^{min} is the same as J_C^{min} for all cases but it is different for the J_S^{max} location. In the cases of tiny and thin workpieces (i.e. $l_w < 3\delta_w$) it is located on the inner surface and close to the ends because of intense edge effect compared to thick workpieces. With increasing workpiece thickness, its position is moved to the middle part and a distance of $\approx 2.5\delta_w$ from the outer surface.

• With increasing the workpiece thickness, J_C increases and reaches a constant value in thick workpieces. For J_S, although J_S^{min} is approximately constant but J_S^{max} decreases with increasing workpiece thickness and becomes constant for $l_w > 2\delta_w$.

• For thick workpiece (i.e. the case of $l_w = 55\ mm$), all effective eddy currents are located in a distance of $\approx 6\delta_w$ from the outer side wall surface and as a result no current in the inner portion.
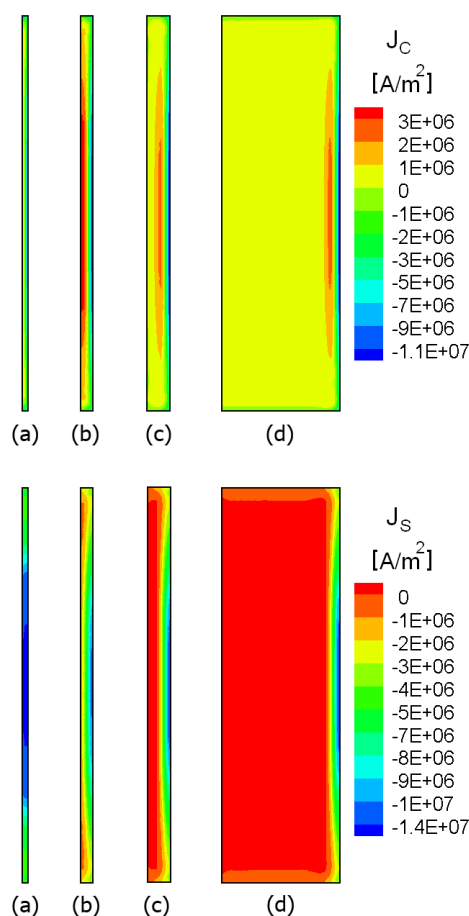
Figure 6: Components of the eddy currents distribution calculated for the workpiece with thickness of (a) $l_w =$ 2 mm ($J_C^{max} = 1.5 \times 10^6$, $J_C^{min} = -8.0 \times 10^6$, $J_S^{max} = -0.45 \times 10^7$, $J_S^{min} = -1.5 \times 10^7$), (b) $l_w = 5$ mm ($J_C^{max} = 4.0 \times 10^6$, $J_C^{min} = -1.2 \times 10^7$, $J_S^{max} = -0.05 \times 10^7$, $J_S^{min} = -1.05 \times 10^7$), (c) $l_w = 10$ mm ($J_C^{max} = 0.25 \times 10^7$, $J_C^{min} = -1.2 \times 10^7$, $J_S^{max} = -0.1 \times 10^7$, $J_S^{min} = -1.1 \times 10^7$) and (d) $l_w = 55$ mm ($J_C^{max} = 0.25 \times 10^7$, $J_C^{min} = -1.2 \times 10^7$, $J_S^{max} = -0.05 \times 10^7$, $J_S^{min} = -1.1 \times 10^7$). The up shows the in-phase component (J_C) and the down shows the out-of-phase component (J_S).

• In most publications devoted to induction heating and induction heat treating [30–32], distribution of eddy current densities along the workpiece thickness is simplified and introduced as being always exponentially decreasing from the surface into the workpiece. This assumption can only be used in induction heating calculations for the purpose of rough engineering estimations. For the cases considered here, the currents density distribution along the radius/thickness has a wave-shaped form (except for tiny workpiece), which is significantly different from the classical exponential distribution. The maximum current density is located at the outer surface. Then the current density decreases toward the core and once it reaches a certain distance from the surface ($\approx 2.5\delta_w$), the current
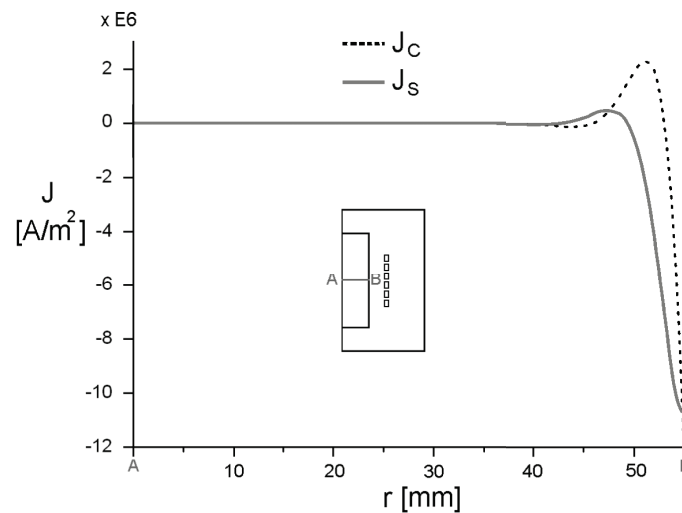
Figure 7: The damped wave-shaped profiles of the eddy currents components along A-B line of the workpiece thickness for the case of $l_w = 55$ mm.

density starts to increase in opposite direction and after reaching a maximum it starts to decrease again.

3.3   Heating pattern

The volumetric heat generation rate (q) in the workpiece has been shown for all cases in Fig. 8. The power intensity is at its maximum value at the middle portion of the outer surface of the workpiece wall (where the J_C^{min} and J_S^{min} are located) and falls off about exponentially inward. The outer surface to core heating difference is a result of the skin effect (the phenomena of nonuniform induced alternative current distribution within the conductor cross section) [30–32]. The most important features are:

• The appearance of varies heating patterns is caused directly by difference in the eddy currents distribution in the workpiece.

• The spatial distribution of heat generation in the induction coil is mostly uniform with local "hot spots" (highly heated areas) at the lowest and upper edges. The skin effect and proximity effect (the effect on current distribution in a conductor when another conductor is placed nearby) are responsible for these hot spots. Since the currents (driving and induced) have the same direction in the coil turns, the eddy currents will be concentrated on opposite side of the induction coil (i.e., the top and lowest surfaces).

• With increasing the workpiece thickness the total heat generation in the workpiece as well as the RF-coil decreases. In other words, the total power generation in the system reduces in thick workpieces. It is worthy to mention that with reduction of total heat generation of the system the coil efficiency (i.e. the part of the energy delivered to the coil that is transferred to the workpiece) decreases too.
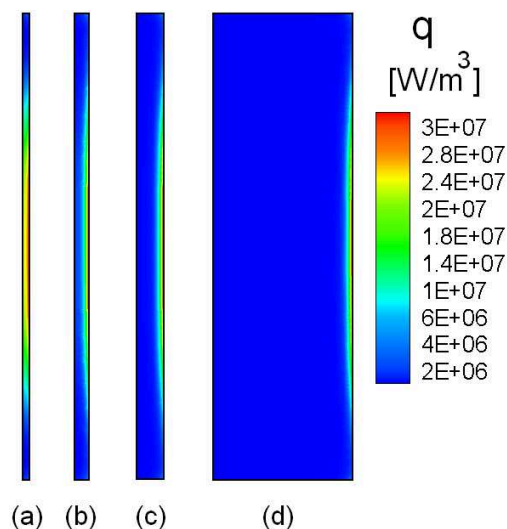
Figure 8: Volumetric power distribution (q) in the workpiece with thickness of (a) $l_w = 2$ mm ($q_{max}^{workpiece} = 3.6 \times 10^7$ W/m^3), (b) $l_w = 5$ mm ($q_{max}^{workpiece} = 3.3 \times 10^7$ W/m^3), (c) $l_w = 10$ mm ($q_{max}^{workpiece} = 3.2 \times 10^7$ W/m^3) and (d) $l_w = 55$ mm ($q_{max}^{workpiece} = 3.0 \times 10^7$ W/m^3). For a better demonstration the workpiece is magnified in the cases of $l_w = 2$ mm and $l_w = 5$ mm.
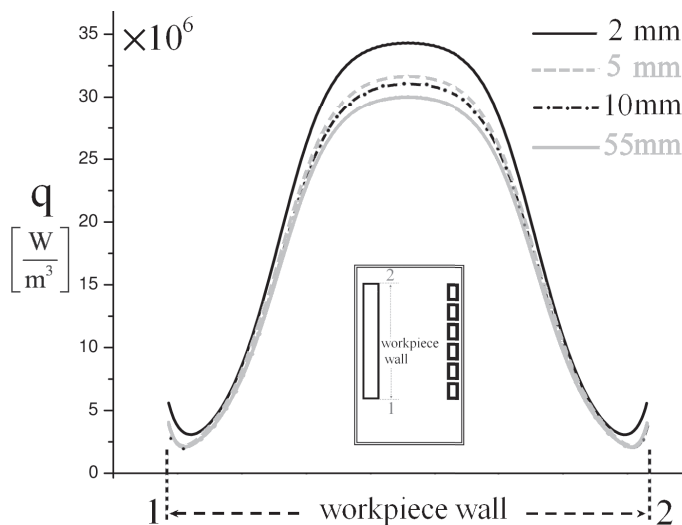
Figure 9: The wave-shaped profiles of the heat generated along the outer surface of the workpiece side wall for the case of (a) $l_w = 2$ mm , (b) $l_w = 5$ mm, (c) $l_w = 10$ mm and (d) $l_w = 55$ mm.

• There are relatively hot spots at the top and bottom corners of the workpiece which are a direct result of edge effect and distortion of electromagnetic filed in those areas, Fig. 9.

Detail information about the heat generated in the system, calculated for different workpiece thicknesses have been shown in Table 3.

Table 3: Detail information about the heat generated in the heating setup, calculated for the cases of $l_w =$ 2,5,10,55 mm workpiece thickness.

Case	Part	Heat generated (*Watt*)	Percentage (%)
$l_w = 2$ mm,	workpiece	2037	63
	RF-coil	1200	37
$l_w = 5$ mm,	workpiece	1416	54
	RF-coil	1204	46
$l_w = 10$ mm,	workpiece	1480	55
	RF-coil	1195	45
$l_w = 55$ mm,	workpiece	1482	55
	RF-coil	1200	45

4 Conclusions

To study the dependence of electromagnetic distribution, eddy currents density and heating pattern on the workpiece thickness, a set of numerical computations was performed. From the obtained results we can conclude:

• The spatial structure of electromagnetic field is a complex function of the workpiece and the RF-coil geometry.

• The eddy currents distribution within the workpiece and RF-coil is not uniform. This current nonuniformity causes a nonuniform heating pattern in the workpiece which in turn leads to a nonuniform temperature profile in the workpiece.

• The induced eddy currents within the workpiece are mostly oriented in the opposite direction of the coil driving current. The maximum value of this opposite currents (J_C^{min} and J_S^{min}) are always located on the outer surface of the workpiece side wall and decrease toward the core as a damped wave-shaped form. After this surface layer ($\sim 2.5\delta_w$) of the workpiece there is an relatively weak eddy current in the same direction of the coil source current. There is no current flow at the center area of the thick workpieces.

• Because the current densities are concentrated in the external areas of workpiece, the resulting heating density is mainly produced in those areas (external heating) and the internal heating (core heating) will be considerably weak for the operating frequency considered here.

References

[1] K. Schönbacher, Zur berechnumg von induktionsöfen, ETZ A, 73 (1952), 735-767.
[2] R.M. Baker, Classical heat flow problems applied to induction billet heating, Trans. AIEE, 77 (1958), 106-112.
[3] P.D. Agarwal, Eddy current losses in solid and laminated iron, AIEE Trans., 78 (1959), 169-179.
[4] A. Mühlbauer, Über die elektrodynamischen kräfte in der schmelze von induktionsöfen, Elektrowärme Int. B, 25 (1967), 461-473.

[5] J.D. Lavers and P.P. Bringer, An analysis of the coreless induction furnace: Axial distribution of electric and magnetic fields, Elektrowärme Int. B, 29 (1971), 232-237.

[6] F. Hegewaldt, Berechnung der stromverdrängung nach einem differenzenverfahren, Paper 632, V. UIE Congress, Wiesbaden (1963).

[7] G. Holmdahl and Y. Sundberg, Berechnung von induktionserwärmung mit digitalrechner, Paper 633, V. UIE Congress, Wiesbaden (1963).

[8] K. Reichert, Die numerische berechnung der elekromagnetisch verursachten strömung in induktionstiegelöfen, Scientia Electrica, XVI (1970), 126-46.

[9] P. Silvester and C.R.S. Haslam, Magnetotelluric modeling by the finite element method, Geophysical Prospecting, 20 (1972), 872-891.

[10] M.V.K. Chari, Finite element solution of the eddy current problem in magnetic structures, IEEE Trans Power App. Syst., 92 (1973), 62-72.

[11] A. Foggia, J.C. Sabonnadiere and P. Silvester , Finite element solution of saturated traveling wave magnetic field problems, IEEE Trans. Power App. Syst., 94 (1975), 866-871.

[12] O. Biro and K. Preis, Finite element analysis of 3-D eddy currents, IEEE Trans. Magnetics, 26 (1990), 418-423.

[13] T. Nakata et al., Investigation of effectiveness of various methods with different unknown variables for 3-D eddy current analysis, IEEE Trans. Magnetics, 26 (1990), 442-445.

[14] T. Nakata et al., Practical analysis of 3-D dynamic nonlinear magnetic field using time periodic finite element method, IEEE Trans. Magnetics, 31 (1995), 1416-1419.

[15] N. Takahashi et al., Investigation of effectiveness of edge elements, IEEE Trans. Magnetics, 28 (1992), 1619-1622.

[16] M.J. Choi and I.H. Park, Transient analysis of magnetodynamic systems using Fourier transform and frequency sensitivity, IEEE Trans. Magnetics, 35 (1999), 1155-1158.

[17] T.H. Fawzi and P.E. Burke, Use of surface integral equations for the analysis of TM-induction problems, Proc. IEE, 121 (1974), 1109-1116.

[18] T.H. Fawzi, K.F. Ali and P.E. Burke, Boundary integral equation analysis of induction devices with rotational symmetry, IEEE Trans. Magnetics, 19 (1983), 36-44.

[19] T. Todaka and M. Enozkizono, Optimal design method with the boundary element method for a high frequency quenching coil, IEEE Trans. Magnetics, 32 (1996), 1262-1265.

[20] L. Pichon and A. Razek, Hybrid finite element and boundary element method using time stepping for eddy current calculation in axisymmetric problems, Proc. IEE, Pt. A, 136 (1989), 217-222.

[21] S. Wasner, L. Krähenbühl and A. Nicolas, Computation of 3D induction hardening problems by combined finite and boundary element methods, IEEE Trans. Magnetics, 30 (1994), 3320-3323.

[22] R. Pascal, P. Conraux and J.M. Bergheau, Coupling between finite elements and boundary elements for the numerical simulation of induction heating processes using a harmonic balance method, IEEE Trans. Magnetics, 39 (2003), 1535-1538.

[23] P. Sergeant et al., Passive and active electromagnetic shielding of induction heaters, IEEE Trans. Magnetics, 40 (2004), 675-678.

[24] T.H. Fawzi, M.T. Ahmed and T.E. Burke, On the use of the impedance boundary conditions in eddy current problems, IEEE Trans. Magnetics, 21 (1985), 1835-1840.

[25] E.M. Deeley and X. Xu, An improved model for a transient surface impedance boundary condition, IEEE Trans. Magnetics, 31 (1995), 1674-1677.

[26] L. Krähenbühl et al., Surface impedances, BIEM and FEM coupled with 1D nonlinear solution to solve 3D high frequency eddy current problems, IEEE Trans. Magnetics, 33 (1997),

1167-1172.

[27] S. Yuferev and L. Kettunen, Implementation of high order surface impedance boundary conditions using vector approximating functions, IEEE Trans. Magnetics, 36 (2000), 1606-1609.

[28] J. Nerg and J. Partanen, A simplified FEM based calculation method for 3-D induction heating problems using surface impedance formulations, IEEE Trans. Magnetics, 37 (2001), 3719-3722.

[29] A. Kost et al., Improvement of nonlinear impedance boundary conditions, IEEE Trans. Magnetics, 38 (2002), 573-576.

[30] A.F. Leatherman and D.E. Stutz, Induction heating advances, National Aeronautics and Space Administration, 1969.

[31] V. Rudnev, D. Loveles, R. Cook and M. Black, Handbook of induction heating, New York NY., 2003.

[32] S. Zinn and S.L. Semiatin, Elements of induction heating, ASM International, 1988.

[33] P.M. Gresho and J.J. Derby, A finite element model for induction heating of a metal crucible, J. Cryst. Growth, 85 (1987), 40-48.

[34] M.H. Tavakoli, Modeling of induction heating in oxide Czochralski systems - advantages and problems, Cryst. Growth Des., 8 (2008), 483-488.

[35] J.R. Reitz, F.J. Milford and R.W. Christy, Foundations of Electromagnetic Theory, Addison-Wesley, 1993.